

## Uniaxial strain tuning of Raman spectra of a ReS<sub>2</sub> monolayer

Iris Niehues<sup>1,\*</sup>,<sup>†</sup> Thorsten Deilmann<sup>2,\*</sup>, Joanna Kutrowska-Girzycka<sup>3</sup>, Alireza Taghizadeh<sup>4</sup>, Leszek Bryja<sup>3</sup>, Ursula Wurstbauer<sup>1</sup>, Rudolf Bratschitsch<sup>1</sup> and Joanna Jadczyk<sup>3</sup>

<sup>1</sup>*Institute of Physics and Center for Nanotechnology, University of Münster, 48149 Münster, Germany*

<sup>2</sup>*Institute of Solid State Theory, University of Münster, 48149 Münster, Germany*

<sup>3</sup>*Department of Experimental Physics, Wrocław University of Science and Technology, 50-370 Wrocław, Poland*

<sup>4</sup>*CAMD, Department of Physics, Technical University of Denmark, 2800 Kgs. Lyngby, Denmark*



(Received 4 December 2021; revised 15 March 2022; accepted 9 May 2022; published 27 May 2022)

In contrast to the intensively investigated transition metal dichalcogenides like MoS<sub>2</sub>, ReS<sub>2</sub> crystals possess a reduced in-plane symmetry, leading to anisotropic optical properties. Here, we report on the impact of strain on the Raman response of a ReS<sub>2</sub> monolayer. Since mechanical strain can be used to shift the Raman-active phonon frequencies, we apply uniaxial tensile strain of up to 0.74% along the Re-chain direction ( $x$  axis) of the atomically thin crystal and measure the Raman response with the scattered light polarized parallel and perpendicular to the strain direction along the  $x$  axis. Complementarily, we carry out *ab initio* calculations to determine the phonon energies and Raman intensities under strain. We find a shift to lower energies for all phonon modes when tensile strain is applied to the monolayer. The determined gauge factors/Grüneisen parameters are in good agreement between experiment and theory. Our study demonstrates that the optomechanical properties of ReS<sub>2</sub> can be tuned by external straining, which is of importance for potential future strain-sensor applications, e.g., in the biomedical sector.

DOI: [10.1103/PhysRevB.105.205432](https://doi.org/10.1103/PhysRevB.105.205432)

### I. INTRODUCTION

Two dimensional (2D) transition metal dichalcogenides (TMDCs) such as MoS<sub>2</sub> and ReS<sub>2</sub> are promising candidates for optomechanical devices due to their outstanding optical and mechanical properties [1–5]. Significant changes in the band structure and the optical properties are observed, when the atomic structure of TMDC crystals is altered by applying mechanical strain [5,6]. For example, strain shifts the exciton energies [1,7] as well as the phonon energies [8,9] of atomically thin semiconductors and changes the exciton phonon coupling in these systems [10,11]. Until now, most of the experimental studies are focused on atomically thin semiconductors with a high in-plane symmetry like  $MX_2$  with  $M = \text{Mo, W}$  and  $X = \text{Se, S}$ . Materials with a lower in-plane symmetry such as ReS<sub>2</sub> and ReSe<sub>2</sub> have gained attention due to their strongly polarized optical response [12–18]. Polarized Raman spectroscopy turned out to be a powerful tool to determine the ReS<sub>2</sub> crystal orientation [17].

Previous studies showed that strain influences the electrical conductance [19], the electron transport [20], or the piezoresistive effect [21] and can lead to a semiconductor to metal transition [22] in ReS<sub>2</sub> monolayers. All these findings make this material a promising candidate for nanoscale strain sensors. However, the influence of strain on the phonon modes, also influencing electronic and transport properties of

ReS<sub>2</sub> monolayers, is so far only investigated by first *ab initio* calculations [23,24] and no systematic strain study has been performed experimentally.

Here, we thoroughly investigate the phonon modes of a ReS<sub>2</sub> monolayer by their Raman response under uniaxial mechanical strain in a combined experiment-theory study. We apply strain in a controlled way [7,10,11] and measure the light inelastically scattered on the phonon modes with polarization parallel and perpendicular to the Re chain ( $x$  axis) of the monolayer. We use *ab initio* calculations to theoretically investigate the energy of the related phonon modes and their strain dependence. These calculations support the assignment to the experimentally observed Raman signatures to specific phonon modes. We find a strain-dependent shift of all investigated phonon modes to lower energies in theory and experiment.

### II. RESULTS

Figure 1(a) shows a schematic view of the ReS<sub>2</sub> crystal structure. In contrast to TMDC monolayers such as MoS<sub>2</sub> and WS<sub>2</sub>, ReS<sub>2</sub> crystals possess a distorted  $1T'$  geometry due to a superlattice structure formed by Re chains [25]. In the following we refer to the axis parallel to these Re chains of the crystal as the  $x$  axis. In previous works it has been found that exfoliated crystals preferably appear in rectangular shapes with a large aspect ratio and the long side parallel to the  $x$  axis of the crystal [12]. In addition, its unique crystal structure leads to a strong anisotropy of the optical properties, e.g., the Raman response, of bulk and thin layers of ReS<sub>2</sub> [12,17]. Our investigated ReS<sub>2</sub> monolayers are micromechanically

\*These two authors contributed equally to this work.

<sup>†</sup>Present address: CIC nanoGUNE BRTA, 20018 Donostia–San Sebastián, Spain; [i.niehues@nanogune.eu](mailto:i.niehues@nanogune.eu)

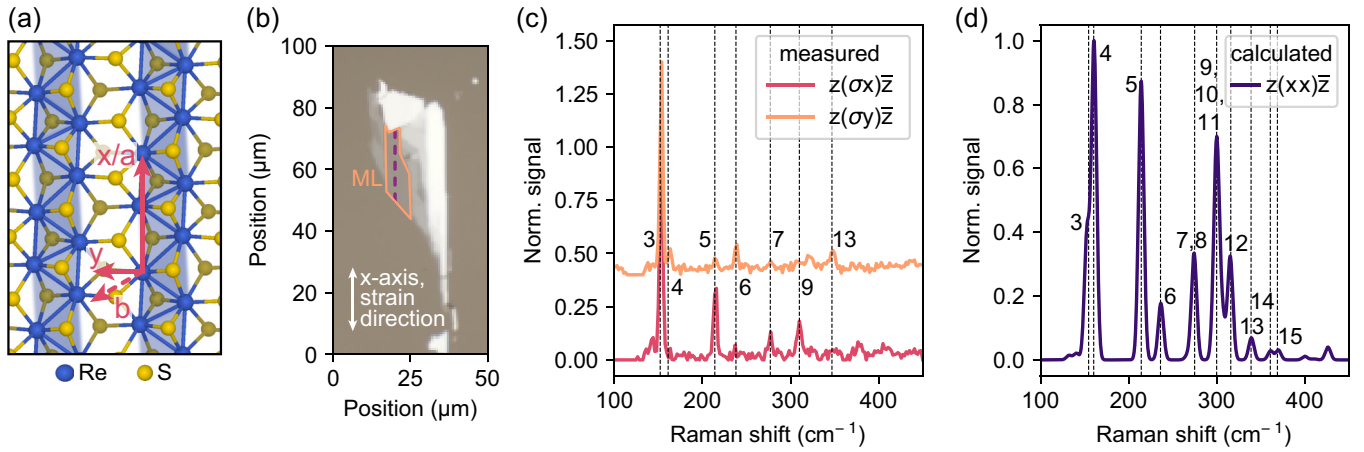


FIG. 1. Raman spectra of a  $\text{ReS}_2$  monolayer. (a) Schematic drawing of the crystal structure highlighting the  $a/x$  and  $b$  axis of the crystal. The  $x$  axis is defined to be parallel to the Re chains. (b) White-light reflection image of the investigated monolayer (outlined in orange) on polycarbonate substrate. The purple line shows the position along which the Raman spectra under strain are recorded. The arrow indicates the  $x$  axis of the crystal as well as the direction of applied uniaxial strain. (c) Measured Raman spectra with polarization of the scattered light parallel [pink,  $z(\sigma_x)\bar{z}$ ] and perpendicular [orange,  $z(\sigma_y)\bar{z}$ ] to the  $x$  axis of the crystal. (d) Calculated Raman spectra for incoming and scattered light polarized parallel to the  $x$  axis  $z(xx)\bar{z}$ . Vertical dashed lines in (c) and (d) mark the position of the different phonon modes. Note that the relative intensities of the Raman modes from experiment and theory displayed in (c) and (d), respectively, cannot be compared directly due to the different polarization.

exfoliated [26] from bulk crystals onto polydimethylsiloxane (PDMS) and are identified by optical reflection microscopy as well as photoluminescence spectroscopy [27] [see Fig. S1 in the Supplemental Material (SM) [28]]. The flakes are then transferred [29] onto a flexible polycarbonate (PC) substrate of  $500\ \mu\text{m}$  thickness. Here, it was taken care that the long side of the monolayer ( $x$  axis) is oriented in such a way on the substrate that it matches the orientation of the applied direction of uniaxial strain. Figure 1(b) shows the white-light reflection image of an investigated monolayer (outlined in orange). All the data shown in the main text have been measured on the same sample in one strain cycle. More samples were investigated to reproduce and verify the obtained results. The purple line indicates the position along which the spectra under strain are recorded. The arrow marks the  $x$  axis of the crystal as well as the direction of applied uniaxial strain. We determine the crystal orientation by measuring the polarization-resolved Raman spectra at zero strain, as shown in Fig. 1(c). To do so, we excite the monolayer with circularly polarized laser light at a wavelength of  $532\ \text{nm}$  and measure the scattered light after passing a  $\lambda/2$  waveplate and linear polarizer. By turning the waveplate, the scattered light polarized parallel (pink) or perpendicular (orange) to the long side of the monolayer is detected (more measurement details can be found in the SM [28]). An additional measurement was performed on the PC substrate in order to determine the background for the measurement (see SM Fig. S2 [28]). For an easier comparison, the spectra are normalized and the orange curve is shifted vertically. The visible phonon modes are marked with dashed vertical lines. In both spectra phonon modes can be identified and we label them according to Ref. [30] (see also Table I). Following Ref. [12] we analyze the polarization of the R5 mode to determine the orientation of the Re-chain axis of the  $\text{ReS}_2$  crystal. While the R5 mode has a maximum intensity for the polarization of the scattered light parallel to the Re

chains ( $x$  axis), it is minimal perpendicular to this [12,17]. It can be seen that the R5 mode almost vanishes in the orange spectrum of Fig. 1(c), while it shows a high intensity in the pink spectrum. Consequently, we identify the pink spectrum in (c) as the one taken parallel to the  $x$  axis [long side of the crystal, parallel to the Re chains,  $z(\sigma_x)\bar{z}$ ] and the orange spectrum is polarized perpendicular [ $z(\sigma_y)\bar{z}$ ] to it. In order to determine the magnitude of the energy shift in the observed phonon modes, we fit the measured Raman spectra with a single Lorentzian for each mode. Exemplary fits of the spectra for

TABLE I. Phonon modes of the  $\text{ReS}_2$  monolayer. Comparison of the modes given in Ref. [30] with the ones measured and calculated in this study for the unstrained case. All values are given in  $\text{cm}^{-1}$ .

Mode	Expt.	Theory	Expt. Ref. [30]
R1	$135.3 \pm 0.5$	132.3	139.2
R2	$141.9 \pm 0.5$	140.6	145.3
R3	$153.7 \pm 0.5$	152.8	153.6
R4	$163.5 \pm 0.5$	160.8	163.6
R5	$214.5 \pm 0.5$	214.3	217.7
R6	$238.0 \pm 0.5$	236.6	237.5
R7	$277.2 \pm 0.5$	267.1	278.3
R8		274.3	284.7
R9	$310.3 \pm 0.5$	297.6	307.8
R10		300.5	311.1
R11		306.9	320.6
R12		315.4	324.9
R13	$348.6 \pm 0.5$	339.4	348.8
R14		361.2	369.5
R15		370.0	377.4
R16		400.1	408.3
R17		410.1	419.3
R18		426.4	437.5

both polarization directions of the scattered light for vanishing strain can be found in SM Fig. S3 [28]. The extracted energies are listed in Table I. We note that the energy of the Raman mode that we assigned to the phonon R9, has a similar energy as the mode labeled R10 in Ref. [30]. However, by comparing the change under strain with theory (see below) an assignment of the mode to the phonon R9 is more plausible. In addition, we calculate the Raman spectra for a freestanding monolayer of ReS<sub>2</sub>. While Raman spectroscopy is versatile and can even be used to identify materials [31], a comprehensive theoretical description of the Raman spectra is challenging [32–35]. For the current work, we limit ourselves to resonant first-order Raman processes which invoke a single phonon which are often the dominant mechanism. Besides the Rayleigh peak (found at the incident frequency  $\omega_{\text{in}}$ ), Stokes and anti-Stokes bands can be found due to inelastic scattering. Separated by the phonon frequency  $\omega_v$  of the  $v$ th phonon, its symmetry determines if a peak is Raman active. The structure of monolayer ReS<sub>2</sub> is characterized by an almost hexagonal unit cell. In this work we employ the experimental structure of  $a = 6.352$  Å,  $b = 6.446$  Å, and  $\gamma = 118.97^\circ$  [36], where the atomic positions are optimized employing density functional theory (DFT) with the Perdew-Burke-Ernzerhof (PBE) functional [37]. Note that the meaning of the  $a$  and  $b$  axis varies in literature. In this work  $a$  is set parallel to the Re chain as shown in Fig. 1(a). As observed before [30], the optimized lattice structure in local density approximation (LDA) would be more compact ( $a = 6.282$  Å,  $b = 6.386$  Å, and  $\gamma = 118.74^\circ$ ), while PBE shows a larger extent ( $a = 6.407$  Å,  $b = 6.515$  Å, and  $\gamma = 118.95^\circ$ ). In all optimizations the forces on each atom are less than  $0.001$  eV/Å [28,38–41].

To calculate the Raman intensity, we follow the approach introduced in Ref. [31]. Both the electron-light and the electron-phonon interaction are treated perturbatively and we restrict ourselves on the system in the ground state that is excited with  $n_v$  phonons. All possible Stokes processes, e.g., absorption of a photon followed by the emission of a phonon and a photon, are summed up and we evaluate the Raman spectrum by

$$I(\omega) = I_0 \sum_v \frac{n_v + 1}{\omega_v} \left| \sum_{\alpha, \beta} u_{\text{in}}^\alpha R_{\alpha, \beta}^v u_{\text{out}}^\beta \right|^2 \delta(\omega - \omega_v). \quad (1)$$

Here,  $I_0$  is a constant (removed in the normalized spectrum),  $u_{\text{in/out}}^\alpha$  are the polarization vectors of the incoming and outgoing field in the direction  $\alpha$ , and  $R_{\alpha, \beta}^v$  denotes the Raman tensor (see Ref. [31] for further details). We employ the excitation wavelength of 532 nm and a temperature of 300 K which is entering in the Bose-Einstein and Fermi-Dirac distribution of phonons and electrons, e.g., the occupation of phonons is given by  $n_v = (\exp[\hbar\omega_v/k_B T] - 1)^{-1}$ . Furthermore, Eq. (1) requires the phonon energies at the  $\Gamma$  point ( $q = 0$ ), and the electron-phonon matrix elements which we evaluate in the first order in atomic displacements [42]. Figure 1(d) shows the calculated Raman spectrum for excitation and scattered light polarized parallel to the  $x$  axis [ $z(xx)\bar{z}$ ]. The theoretical results show 18 different active phonon modes with the irreducible representation  $A_g$ , similar as observed in previous results [24,30]. The frequencies of all these modes are listed

in Table I. The 18  $A_u$  modes which do not couple to light are not further discussed here.

Overall, our calculations agree very well with the experimentally observed Raman-active phonon modes and the ones measured by Feng *et al.* [30]. However, a slight energy shift to lower energies for the modes at higher energy is observed in our calculation compared to the measurement. This deviation is a result of the employed lattice structure as well as the chosen functional as already discussed in [30]. Furthermore, the substrate has not been taken into account in our calculations. We want to stress that the theoretically obtained relative shifts under strain investigated in the following are much less affected by the just mentioned factors. In our test calculations for different lattice structures such shifts typically deviate by less than 10%. To calculate the strain-dependent energetic positions of the Raman peaks, we apply tensile strain along the  $x$  axis (i.e., along the Re chain) using the Poisson ratio of 0.225 [43]. Similar to our previous studies [7,10] we repeat the structural optimization for the new cell parameters, i.e., we allow for atomic relaxations. For the small strain values applied in this work, we find a linear shift of the considered phonon energies, i.e., finally of the Raman maxima.

In the experiment, we apply uniaxial strain of up to 0.74% to the ReS<sub>2</sub> monolayer after determining the crystal orientation and identifying the phonon modes in the measured spectra. As shown in Figs. 1(b) and 1(c), we have confirmed that we indeed apply uniaxial strain parallel to the Re chains of the ReS<sub>2</sub> monolayer. By bending the substrate in a controlled way, we apply tensile strain values to the monolayer [7,10,44]. For every applied strain level, Raman spectra are recorded with emission polarization of the scattered light perpendicular and parallel to the  $x$  axis/strain direction. It is well known from TMDC mono- and bilayers that the strain is not transferred homogeneously from the substrate to the crystal. The strain rather increases from the sample edges towards the center and reaches a constant and maximum strain transfer several micrometers from the edges [7,11]. Therefore, it is crucial to determine the positions on the flake providing maximum strain transfer. To this end, we record Raman spectra in  $2 \mu\text{m}$  steps along the vertical dashed line in Fig. 1(b) for each strain value. Figure 2(a) displays the R3 mode along the flake with parallel polarization [ $z(\sigma x)\bar{z}$ ]. The position with  $0 \mu\text{m}$  indicates the bottom edge of the monolayer in Fig. 1(b). The first Raman spectrum is measured  $2 \mu\text{m}$  from the bottom edge. The last measured position is at the top edge of the monolayer. The different strain levels are color-coded with a minimum strain of 0.00% (dark purple) and a maximum strain of 0.74% (yellow). In the unstrained case (dark purple) the R3 mode varies slightly over the entire flake by approximately  $\pm 0.5 \text{ cm}^{-1}$  (e.g., at the position of  $22 \mu\text{m}$  the value is  $152.8 \text{ cm}^{-1}$ ). With increasing strain values, the R3 mode shows a shift to lower energies with a nearly constant value between 12 and  $30 \mu\text{m}$  indicating a full strain transfer in this region [7,11]. We therefore use the position at  $22 \mu\text{m}$  (marked with the blue line) to investigate the shift of all visible phonon modes under strain since this position is in the middle of the full strain transfer region. We would like to note that analyzing different positions between 12 and  $30 \mu\text{m}$  lead to the same results within the experimental resolution (Fig. S4 in the SM). The extracted values for the shift of the phonon mode R3 at

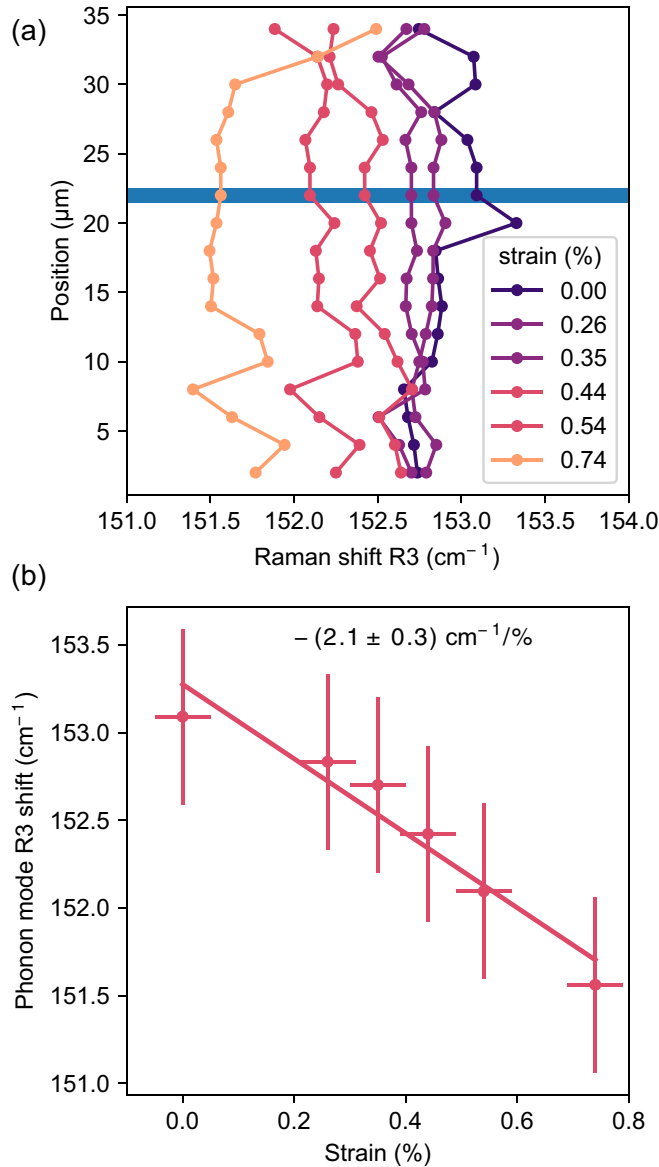


FIG. 2. R3 mode under strain. (a) Spatially resolved phonon energy shift of the R3 mode along the flake, where the position at  $0 \mu\text{m}$  indicates the bottom edge of the monolayer in Fig. 1(b). The different strain levels are color coded from purple to yellow. The blue line at  $22 \mu\text{m}$  marks the position on the flake where the Raman shifts under strain are investigated. (b) Extracted energy values of the R3 mode as a function of strain at the position marked in (a). A gauge factor of  $-(2.1 \pm 0.3) \text{ cm}^{-1}/\%$  is determined.

$22 \mu\text{m}$  are exemplarily plotted against the applied uniaxial strain in Fig. 2(b). With increasing strain, a shift of the mode energy to lower energies is visible. A linear behavior of the strain-induced shift is evident, with the slope from the linear regression being  $-(2.1 \pm 0.3) \text{ cm}^{-1}/\%$ . This quantity will be named gauge factor from here on. Following Ref. [44] we can calculate the corresponding Grüneisen parameter of this mode to  $\gamma = 1.76 \pm 0.25$  [28].

In order to analyze the effect of strain in the experiment, we extract the gauge factors, i.e., the energy shift, for all

TABLE II. Comparison of the experimentally observed gauge factors under uniaxial strain for all phonon modes of the  $\text{ReS}_2$  monolayer. The strain is applied parallel to the direction of the  $x$  axis (Re chain). The theoretical values are obtained by DFT calculations. Due to the uncertainty of the used Poisson ratio, we expect an error of up to  $0.1 \text{ cm}^{-1}/\%$ . The experimental values are extracted from the measurements with the polarization of the scattered light parallel and perpendicular to the  $x$  axis. Fits to the experimental data can be found in the SM Figs. S5 and S6 [28]. All values are given in  $\text{cm}^{-1}/\%$ .

Mode	Theory	Expt. $z(\sigma x)\bar{z}$	Expt. $z(\sigma y)\bar{z}$
R1	-0.6		
R2	-2.2		
R3	-1.4	$-2.1 \pm 0.3$	$-2.2 \pm 0.2$
R4	-1.3		$-1.9 \pm 0.4$
R5	-2.8	$-3.0 \pm 0.5$	
R6	-0.7		$-2.0 \pm 0.41$
R7	-3.1	$-3.0 \pm 0.3$	
R8	-1.0		
R9	-1.2	$-2.3 \pm 0.5$	
R10	-0.1		
R11	-1.1		
R12	-1.5		
R13	-1.9		$-2.2 \pm 0.5$
R14	-4.2		
R15	-2.5		
R16	-1.4		
R17	-0.8		
R18	-0.3		

visible modes as already exemplarily shown for the R3 mode in Fig. 2(b) for the  $z(\sigma x)\bar{z}$  direction (see SM Fig. S5 and Fig. S6 for the corresponding fits [28]) and list the shifts in Table II (the corresponding Grüneisen parameters are listed in the SM [28]). The mode R3 can be analyzed in both emission polarization directions used in the experiment. It can be seen that the observed change under strain is the same for both polarizations of the scattered light. Note that these shifts depend on the direction in which the strain is applied. While we are only able to apply strain along the  $x$  axis in the experiment, our calculations reveal, for instance, a shift of  $-2.3 \text{ cm}^{-1}/\%$  for R3 if the strain is applied along the  $b$  axis.

Besides the energetic shifts, our calculations also predict relative changes of the intensities due to the applied strain. However, for the applied strain values ( $< 1\%$ ) these changes are typically small, i.e., up to about 3%. For modes with higher intensities, e.g., R3 vs R5, we find changes up to 10%. Compared to the variation of the intensities at different spatial positions in the experiment, such small variations are currently challenging to verify.

Figure 3 shows the calculated and measured phonon modes under strain. The purple lines represent the calculated energy positions for strain values between 0% and 1%. Pink dots mark the experimental values determined from the Raman spectra measured with polarization parallel to the  $x$  axis [ $z(\sigma x)\bar{z}$ ]; yellow crosses show the data from the perpendicular polarization [ $z(\sigma y)\bar{z}$ ] measurement. Due to the energy offset between theory and experiment for modes R4 and higher than

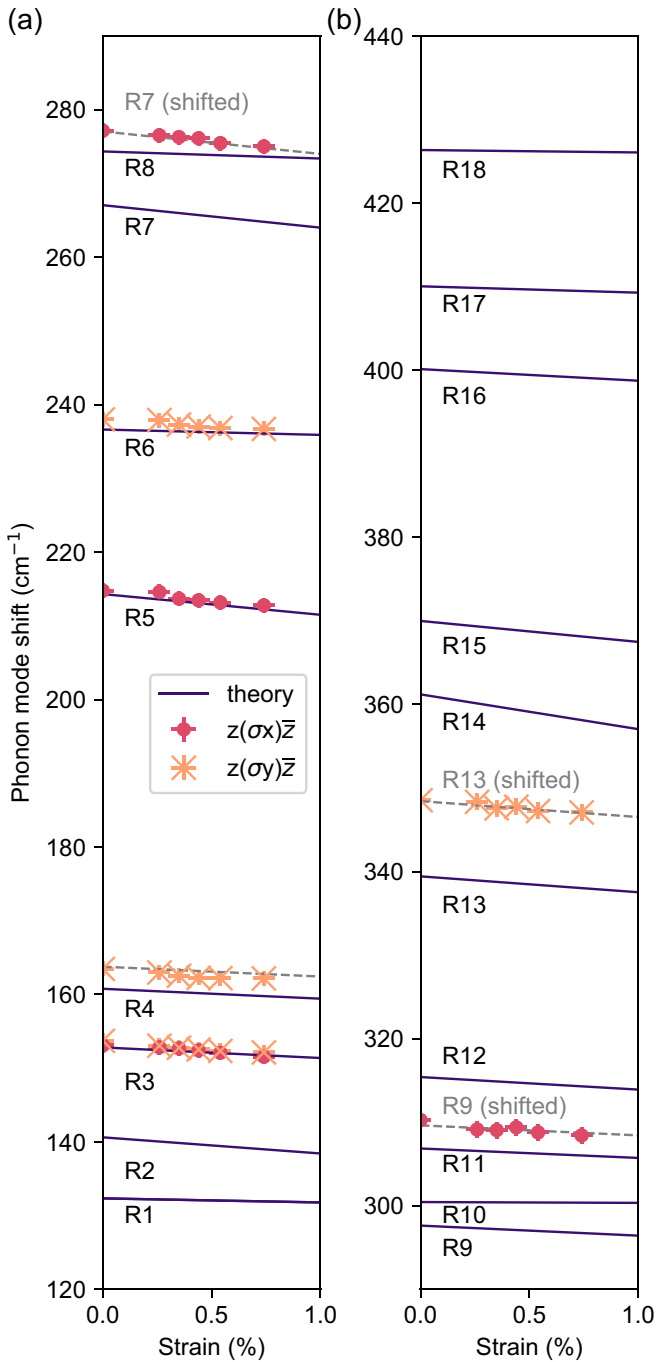


FIG. 3. Phonon modes under uniaxial strain. Shift of the phonon modes R1–R8 (a) and R9–R18 (b). The calculated phonon energy shifts are shown as lines. Pink dots show the experimental values determined from the Raman spectra measured with polarization parallel to the  $x$  axis; yellow crosses show the data from the perpendicular measurement. Due to the energy offset between theory and experiment for the R4 mode and modes higher than R8, the calculated shifts for these modes (R4, R7, R9, and R13) are additionally plotted as dashed gray lines for better comparison.

R8 (see Table I and discussion above) we also plot the shifted theoretical predictions which match the experimental values as gray dashed lines as a guide to the eye. It is visible that the experimentally observed strain-induced shifts of the phonon modes have negative gauge factors for increasing tensile strain and nicely follow the theoretical predictions in Table II). An overall good agreement is found between experiment and theory. In detail, we find slightly stronger deviations for the position of higher energy phonon modes in the experiment with respect to our calculations (Table I). This might be a result of the substrate which is missing in our calculation that could lead to a steeper potential.

### III. CONCLUSIONS

In conclusion, we have systematically investigated the shift of phonon modes of  $\text{ReS}_2$  monolayers under strain determined by Raman spectroscopy and *ab initio* calculations. With applied uniaxial tensile strain parallel to the  $x$  axis (Re chain) of the crystal we measured the scattered light and determined the phonon mode energies for each mode. By taking care of the spatially dependent strain transfer from the substrate to the monolayer we found a shift to lower energies for all the visible Raman-active modes. We compared our results with DFT calculations, where strain-induced energy shifts for all 18 phonon modes have been predicted. All modes exhibit a shift to lower energies with gauge factors lying between  $-0.1 \text{ cm}^{-1}/\%$  and  $-4.2 \text{ cm}^{-1}/\%$  (corresponding to Grüneisen parameters between 0.04 and 1.50). We found a good agreement between the measured and calculated shifts.

Our work demonstrates that mechanical strain is a suitable tool to control the phonon modes of a  $\text{ReS}_2$  monolayer and represents an important step towards its application in strain devices [45]. The application of strain could be used to alter the highly anisotropic thermal conductivity in  $\text{ReS}_2$  [46] that is of importance for the heat management and thermoelectric properties in  $\text{ReS}_2$ -based circuitries.

### ACKNOWLEDGMENTS

The project was supported by the Polish NAWA under an APM Grant No. PPI/APM/2019/1/00085/U/00001. We thank Paweł Machnikowski for making this project possible and Daniel Wigger for fruitful discussions. We thank Ching-Hwa Ho from Graduate Institute of Applied Science and Technology, National Taiwan University of Science and Technology, Taipei 106, Taiwan for providing the  $\text{ReS}_2$  bulk crystals. T.D. acknowledges financial support from the German Research Foundation (DFG Project No. DE 2749/2-1) and computing time granted by the John von Neumann Institute for Computing (NIC) and provided on the super-computer JUWELS at the Jülich Supercomputing Centre (JSC). J.J. and J.K.-G. acknowledge support by the Polish National Science Center (NCN) Grant OPUS 19 No. 2020/37/B/ST3/00539.

[1] R. Roldan, A. Castellanos-Gomez, E. Cappelluti, and F. Guinea, Strain engineering in semiconducting two-dimensional crystals, *J. Phys.: Condens. Matter* **27**, 313201 (2015).

[2] G. Plechinger, A. Castellanos-Gomez, M. Buscema, Herre S. J. Van Der Zant, G. A. Steele, A. Kuc, T. Heine, C. Schueller, and T. Korn, Control of biaxial strain in single-layer molybdenite

- using local thermal expansion of the substrate, *2D Mater.* **2**, 015006 (2015).
- [3] A. Castellanos-Gomez, Why all the fuss about 2D semiconductors? *Nat. Photon.* **10**, 202 (2016).
- [4] T. Mueller and E. Malic, Exciton physics and device application of two-dimensional transition metal dichalcogenide semiconductors, *npj 2D Mater. Appl.* **2**, 29 (2018).
- [5] Y. Liu, X. Li, Y. Guo, T. Yang, K. Chen, C. Lin, J. Wei, Q. Liu, Y. Lu, L. Dong *et al.*, Modulation on the electronic properties and band gap of layered ReSe<sub>2</sub> via strain engineering, *J. Alloys Compd.* **827**, 154364 (2020).
- [6] F. Carrascoso, H. Li, R. Frisenda, and A. Castellanos-Gomez, Strain engineering in single-, bi- and tri-layer MoS<sub>2</sub>, MoSe<sub>2</sub>, WS<sub>2</sub> and WSe<sub>2</sub>, *Nano Res.* **14**, 1698 (2021).
- [7] R. Schmidt, I. Niehues, R. Schneider, M. Drüppel, T. Deilmann, M. Rohlfing, S. Michaelis de Vasconcellos, A. Castellanos-Gomez, and R. Bratschitsch, Reversible uniaxial strain tuning in atomically thin WSe<sub>2</sub>, *2D Mater.* **3**, 021011 (2016).
- [8] H. J. Conley, B. Wang, J. I. Ziegler, R. F. Haglund, Jr., S. T. Pantelides, and K. I. Bolotin, Bandgap engineering of strained monolayer and bilayer MoS<sub>2</sub>, *Nano Lett.* **13**, 3626 (2013).
- [9] C. R. Zhu, G. Wang, B. L. Liu, X. Marie, X. F. Qiao, X. Zhang, X. X. Wu, H. Fan, P. H. Tan, T. Amand, and B. Urbaszek, Strain tuning of optical emission energy and polarization in monolayer and bilayer MoS<sub>2</sub>, *Phys. Rev. B* **88**, 121301(R) (2013).
- [10] I. Niehues, A. Blob, T. Stiehm, R. Schmidt, V. Jadriško, B. Radatović, D. Čapeta, M. Kralj, S. Michaelis de Vasconcellos, and R. Bratschitsch, Strain transfer across grain boundaries in MoS<sub>2</sub> monolayers grown by chemical vapor deposition, *2D Mater.* **5**, 031003 (2018).
- [11] I. Niehues, P. Marauhn, T. Deilmann, D. Wigger, R. Schmidt, A. Arora, S. Michaelis de Vasconcellos, and R. Bratschitsch, Strain tuning of the Stokes shift in atomically thin semiconductors, *Nanoscale* **12**, 20786 (2020).
- [12] D. A. Chenet, O. B. Aslan, P. Y. Huang, C. Fan, A. M. van der Zande, T. F. Heinz, and J. C. Hone, In-plane anisotropy in mono- and few-layer ReS<sub>2</sub> probed by Raman spectroscopy and scanning transmission electron microscopy, *Nano Lett.* **15**, 5667 (2015).
- [13] A. Arora, J. Noky, M. Drüppel, B. Jariwala, T. Deilmann, R. Schneider, R. Schmidt, O. D. Pozo-Zamudio, T. Stiehm, A. Bhattacharya *et al.*, Highly anisotropic in-plane excitons in atomically thin and bulklike 1T-ReS<sub>2</sub>, *Nano Lett.* **17**, 3202 (2017).
- [14] A. McCreary, J. R. Simpson, Y. Wang, D. Rhodes, K. Fujisawa, L. Balicas, M. Dubey, V. H. Crespi, M. Terrones, and A. R. Hight Walker, Intricate resonant Raman response in anisotropic ReS<sub>2</sub>, *Nano Lett.* **17**, 5897 (2017).
- [15] S. Zhang, N. Mao, N. Zhang, J. Wu, L. Tong, and J. Zhang, Strain-engineering the anisotropic electrical conductance in ReS<sub>2</sub> monolayer, *ACS Nano* **11**, 10366 (2017).
- [16] J. Jadcak, J. Kutrowska-Girzycka, T. Smolenski, P. Kossacki, Y. S. Huang, and L. Bryja, Exciton binding energy and hydrogenic Rydberg series in layered ReS<sub>2</sub>, *Sci. Rep.* **9**, 1578 (2019).
- [17] Y. Choi, K. Kim, S. Y. Lim, J. Kim, J. M. Park, J. H. Kim, Z. Lee, and H. Cheong, Complete determination of the crystallographic orientation of ReX<sub>2</sub> (X = S, Se) by polarized Raman spectroscopy, *Nanoscale Horiz.* **5**, 308 (2020).
- [18] J. Wang, Y. J. Zhou, D. Xiang, S. J. Ng, K. Watanabe, T. Taniguchi, and G. Eda, Polarized light-emitting diodes based on anisotropic excitons in few-layer ReS<sub>2</sub>, *Adv. Mater.* **32**, 2001890 (2020).
- [19] S. Yu, H. Zhu, K. Eshun, C. Shi, M. Zeng, and Q. Li, Strain-engineering the anisotropic electrical conductance in ReS<sub>2</sub> monolayer, *Appl. Phys. Lett.* **108**, 191901 (2016).
- [20] Y.-C. Lin, H.-P. Komsa, C.-H. Yeh, T. Bjorkman, Z.-Y. Liang, C.-H. Ho, Y.-S. Huang, P.-W. Chiu, A. V. Krasheninnikov, and K. Suenaga, Single-layer ReS<sub>2</sub>: Two-dimensional semiconductor with tunable in-plane anisotropy, *ACS Nano* **9**, 11249 (2015).
- [21] C. An, W. S. Zhihao Xu, R. Zhang, Z. Sun, S. Tang, Y.-F. Xiao, D. Zhang, D. Sun, X. Hu, C. Hu *et al.*, The opposite anisotropic piezoresistive effect of ReS<sub>2</sub>, *ACS Nano* **13**, 3310 (2019).
- [22] P. C. Sreeparvathy, V. Kanchana, P. Anees, and G. Vaitheeswaran, Emergence of strain induced two dimensional metallic state in ReS<sub>2</sub>, *J. Solid State Chem.* **269**, 138 (2019).
- [23] T.-H. Li, Z.-H. Zhou, J.-H. Guo, and F.-R. Hu, Raman scattering modification in monolayer ReS<sub>2</sub> controlled by strain engineering, *Chin. Phys. Lett.* **33**, 046201 (2016).
- [24] M. Yagmurcukardes, C. Bacaksiz, E. Unsal, B. Akbali, R. T. Senger, and H. Sahin, Strain mapping in single-layer two-dimensional crystals via Raman activity, *Phys. Rev. B* **97**, 115427 (2018).
- [25] J. C. Wildervanck and F. Jelinek, The dichalcogenides of technetium and rhenium, *J. Less-Common Met.* **24**, 73 (1971).
- [26] P. Tonndorf, R. Schmidt, P. Böttger, X. Zhang, J. Börner, A. Liebig, M. Albrecht, C. Kloc, O. Gordan, D. R. T. Zahn *et al.*, Photoluminescence emission and Raman response of monolayer MoS<sub>2</sub>, MoSe<sub>2</sub>, and WSe<sub>2</sub>, *Opt. Express* **21**, 4908 (2013).
- [27] S. Tongay, H. Sahin, C. Ko, A. Luce, W. Fan, K. Liu, J. Zhou, Y.-S. Huang, C.-H. Ho, J. Yan *et al.*, Monolayer behaviour in bulk ReS<sub>2</sub> due to electronic and vibrational decoupling, *Nat. Commun.* **5**, 3252 (2014).
- [28] See Supplemental Material at <http://link.aps.org/supplemental/10.1103/PhysRevB.105.205432> for further details.
- [29] A. Castellanos-Gomez, M. Buscema, R. Molenaar, V. Singh, L. Janssen, H. S. J. Van Der Zant, and G. A. Steele, Deterministic transfer of two-dimensional materials by all-dry viscoelastic stamping, *2D Mater.* **1**, 011002 (2014).
- [30] Y. Feng, W. Zhou, Y. Wang, J. Zhou, E. Liu, Y. Fu, Z. Ni, X. Wu, H. Yuan, F. Miao *et al.*, Raman vibrational spectra of bulk to monolayer ReS<sub>2</sub> with lower symmetry, *Phys. Rev. B* **92**, 054110 (2015).
- [31] A. Taghizadeh, U. Leffers, T. G. Pedersen, and K. S. Thygesen, A library of ab initio Raman spectra for automated identification of 2D materials, *Nat. Commun.* **11**, 3011 (2020).
- [32] J. B. Renucci, R. N. Tyte, and M. Cardona, Resonant Raman scattering in silicon, *Phys. Rev. B* **11**, 3885 (1975).
- [33] C. Ambrosch-Draxl, H. Auer, R. Kouba, E. Ya Sherman, P. Knoll, and M. Mayer, Raman scattering in YBa<sub>2</sub>C<sub>3</sub>O<sub>7</sub>: A comprehensive theoretical study in comparison with experiments, *Phys. Rev. B* **65**, 064501 (2002).
- [34] Y. Gillet, S. Kontur, M. Giantomassi, C. Draxl, and X. Gonze, *Ab initio* approach to second-order resonant Raman scattering including exciton-phonon interaction, *Sci. Rep.* **7**, 7344 (2017).
- [35] S. Reichardt and L. Wirtz, Theory of resonant Raman scattering: Towards a comprehensive *ab initio* description, *Phys. Rev. B* **99**, 174312 (2019).

- [36] H.-J. Lamfers, A. Meetsma, G. A. Wiegers, and J. L. de Boer, The crystal structure of some rhenium and technetium dichalcogenides, *J. Alloys Compd.* **241**, 34 (1996).
- [37] J. P. Perdew, K. Burke, and M. Ernzerhof, Generalized Gradient Approximation Made Simple, *Phys. Rev. Lett.* **77**, 3865 (1996).
- [38] J. A. Majewski and P. Vogl, Self-interaction-corrected density-functional formalism. I. Ground-state properties of the Hubbard-Peierls model, *Phys. Rev. B* **46**, 12219 (1992).
- [39] J. Wierferink, P. Krüger, and J. Pollmann, Improved hybrid algorithm with Gaussian basis sets and plane waves: First-principles calculations of ethylene adsorption on  $\beta$ -SiC(001)-(3  $\times$  2), *Phys. Rev. B* **74**, 205311 (2006).
- [40] A. H. Larsen, J. J. Mortensen, J. Blomqvist, I. E. Castelli, R. Christensen, M. Dułak, J. Friis, M. N. Groves, B. Hammer, C. Hargus *et al.*, The atomic simulation environment—a python library for working with atoms, *J. Phys.: Condens. Matter* **29**, 273002 (2017).
- [41] J. Enkovaara, C. Rostgaard, J. J. Mortensen, J. Chen, M. Dułak, L. Ferrighi, J. Gavnholt, C. Glinsvad, V. Haikola, H. A. Hansen *et al.*, Electronic structure calculations with GPAW: A real-space implementation of the projector augmented-wave method, *J. Phys.: Condens. Matter* **22**, 253202 (2010).
- [42] F. Giustino, Electron-phonon interactions from first principles, *Rev. Mod. Phys.* **89**, 015003 (2017).
- [43] H. Wang, E. Liu, Y. Wang, B. Wan, C.-H. Ho, F. Miao, and X. G. Wan, Cleavage tendency of anisotropic two-dimensional materials: ReX<sub>2</sub> (X = S, Se) and WTe<sub>2</sub>, *Phys. Rev. B* **96**, 165418 (2017).
- [44] T. Mohiuddin, A. Lombardo, R. R. Nair, A. Bonetti, G. Savini, R. Jalil, N. Bonini, D. M. Basko, C. Galiotis, N. Marzari *et al.*, Uniaxial strain in graphene by Raman spectroscopy: G peak splitting, Grüneisen parameters, and sample orientation, *Phys. Rev. B* **79**, 205433 (2009).
- [45] A. C. Ferrari, F. Bonaccorso, V. Fal'Ko, K. S. Novoselov, S. Roche, P. Bøggild, S. Borini, F. H. L. Koppens, V. Palermo, N. Pugno *et al.*, Science and technology roadmap for graphene, related two-dimensional crystals, and hybrid systems, *Nanoscale* **7**, 4598 (2015).
- [46] H. Jang, C. R. Ryder, J. D. Wood, M. C. Hersam, and D. G. Cahill, 3D anisotropic thermal conductivity of exfoliated rhenium disulfide, *Adv. Mater.* **29**, 1700650 (2017).